Magnetic phase transitions in an electroelastic model for magnetically ordered spin-crossover solids

S. B. Ogou,[1] T. D. Oke,[1,2,*] F. Hontinfinde,[1] and K. Boukheddaden [2,†]

[1]*Département de Physique (FAST) et Institut des Mathématiques et de Sciences Physiques (IMSP),*
Université d'Abomey-Calavi, 01 BP 613, Porto-Novo, Benin
[2]*Université Paris-Saclay, UVSQ, CNRS, GEMAC UMR 8635, 45 Avenue des Etats Unis, F78035 Versailles Cedex, France*

Spin-crossover and Prussian blue analog materials are investigated in two dimensions with the three-state Blume-Emery-Griffiths model where each spin interacts with its nearest neighbors and next-nearest neighbors and may be either in high-spin or low-spin state. The interactions through the system are strongly dependent on the instantaneous distance between atoms and are magnetic and elastic in nature. Finite-size effects have been detected at finite temperature on the model. The thermal distortion of the lattice configuration due to lattice unit displacements strengthened the thermal spin transition that occurred. The generated numerical results are obtained by two-step Monte Carlo simulations where used thermodynamic parameters allowed to establish a rich phase diagram. Gradual and first-order transitions with thermally induced hysteresis phenomena have been observed. Near the thermal hysteresis loops, the model exhibits throughout relaxation curves lattice configurations evolving through two-dimensional nucleation and growth processes that are enhanced with suitable values of the model parameters.

I. INTRODUCTION

Molecular-based materials as spin-crossover (SCO) solids and Prussian blue analogs (PBAs) [1] constitute a class of very promising materials with real opportunities of applications (in various domains of material science) as display and memory devices [1–4], multisensors [5–14], probes of contact pressure or shocks [15], as well as actuators [6,16–18]. They are commutable solids with the presence of transition metal coordination which have an electronic configuration ranging between $3d^4$ and $3d^7$ (chromium, manganese, iron, and cobalt) in octahedral symmetry, surrounded by nitrogen atoms, called SCO complexes [1,19–22]. In special conditions, they may exhibit a phase transition between the diamagnetic low-spin (LS) state and the paramagnetic high-spin (HS) state [23–25] under external stimuli such as light, pressure, temperature, magnetic, and electric fields, etc. [23–26]. The thermally induced spin transition leads to both electronic and structural changes, often observed as a color and magnetic moment changes [1,27,28]. The system properties are strongly dependent on interactions between molecules. For weak interactions, the HS fraction changes smoothly with the temperature; whereas when they become strong enough, the system exhibits cooperative phenomena [29–31] which manifest through the existence of first-order transitions accompanied with thermal hysteresis. Then, the change in HS fraction becomes sharper and sharper with increasing interaction strength between molecules. Of course, the interaction in SCO solids is dominated by the variations of unit-cell volume and bond length, that are considerably larger in the HS state.

The most common case studied in literature is of Fe(II)-based SCO materials with $3d^6$ configuration where the total true spin equal to $S = 2$ and 0 in HS and LS states, respectively. The SCO phenomenon is the result of the redistribution of the electrons between the bonding t_{2g} and the antibonding e_g orbitals. In the diamagnetic ($S = 0$) LS state, only bonding orbitals are populated ($t_{2g}^6 e_g^0$), while in the paramagnetic ($S = 2$) HS state, the electronic configuration becomes ($t_{2g}^4 e_g^2$) according to the Hund's rule. The microscopic changes of the magnetoelastic properties of the SCO solids at the transition accompanied with large volume changes resulting from the constructive interferences of the molecular volume changes which deploy at long range through elastic interactions. As well demonstrated in several works [29,30,32], the elastic interactions are at the heart of the existence of cooperative effects in SCO materials and play a crucial role in the existence of first-order transitions and thermally induced hysteresis loops observed experimentally [29]. Novel properties [33–35] have been also detected for SCO solids, in particular, the combination of magnetoelastic, photochromic, thermochromic, and photoluminescence (PL) features [36–46] in the same material.

In this work, materials combining the spin-transition phenomenon with ferromagnetic interactions are investigated. Describing this particular SCO system, we used the Blume-Emery-Griffiths (BEG) models [47–49] in which we accounted for the elastic and magnetic interactions [34,50–62]. We demonstrate that the magnetic and elastic interactions generate tremendous changes in the spin-transition properties, bringing to light unique and unprecedented nonlinear behaviors of the HS fraction n_{HS}. We study carefully the competitions of the elasticlike interactions responsible for the existence of multistep transitions and reentrant phase transitions triggered by the magnetic interactions [52,54,55,57,58,63–

*Corresponding author: toussaint.oke@imsp-uac.org
†Corresponding author: kamel.boukheddaden@uvsq.fr

67]. A detailed study of the system properties allowed to establish a rich phase diagram [68,69] in which the various system phases have been identified. Moreover, a dynamical version of the present model based on a master-equation treatment of the Hamiltonian is also presented [70–72]. There, we studied the relaxation of the metastable high-spin states at low temperature as well as the dynamical behavior at finite temperature in bistability regions.

The paper is organized as follows. In Sec. II, we define the Hamiltonian model of the system and present its included interactions as magnetoelastic and electronic parts which are responsible of the system structure and spin-state modifications. Section III is devoted to the two-step Monte Carlo algorithm used on the spin state and for the displacements of the lattice sites. Section IV contains the discussions of the obtained results with the model parameters which are described in the Hamiltonian. In the last section, we conclude.

II. MODEL DESCRIPTION AND INTERACTION HAMILTONIAN

This work is inspired from the electroelastic model of Boukheddaden *et al.* [50–55], designed to describe the thermally induced first-order transition in spin-crossover models accounting for their electronic and volume changes at the transition. The electroelastic model was based on the study of a two-dimensional (2D) lattice of SCO atoms coupled elastically through springs whose elastic constants and equilibrium distances depend on the spin states of the connected sites. In such a model, the spin-transition molecule is described with a fictitious spin σ, whose values -1 and $+1$ associated to the low-spin (diamagnetic) and high-spin (paramagnetic) states. As a matter of fact, this model does not include any ferromagnetic interactions between the spin states, and the HS spin state is then paramagnetic. Recent developments in the chemistry of spin-crossover materials and switchable solids [6,73,74] revealed a original type of SCO materials which order magnetically in the HS phase (at low temperature). In these systems, the exchange (or superexchange) interactions between the spin states in the HS state are then at work. Besides, the magnetic exchange interaction was introduced inside binuclear SCO complexes [75] together with an Ising-type interaction coupling between the binuclear units. To extend our previous two-state electroelastic model to study the case of ferromagnetic SCO materials, we designed a spin-1 BEG model that takes into account electroelastic interactions [50–53] between SCO units based on three-state fictitious spin description of a deformable lattice with square symmetry of size L. The spin variables at each lattice site can be in HS state with $S_i = \pm 1$ (magnetic state) or in LS state $S_i = 0$ (nonmagnetic state). The degeneracy ratio between HS and LS states is defined by $g = g_{HS}/g_{LS}$, where g_{HS} and g_{LS} are the degeneracies of the HS and LS states, respectively. Here, we take $g = 150$, which leads to a molar entropy change at the transition $\Delta S = R \ln g \simeq 41.7 \text{ J K}^{-1} \text{ mol}^{-1}$, which is in fair agreement with experimental data of literature [31,76]. SCO molecules are assumed to elastically interact via springs and the lattice deformation is assumed to remain inside the plane (see Fig. 1). Thus, the topological structure of bonds between atomic sites will be conserved during the simulations.
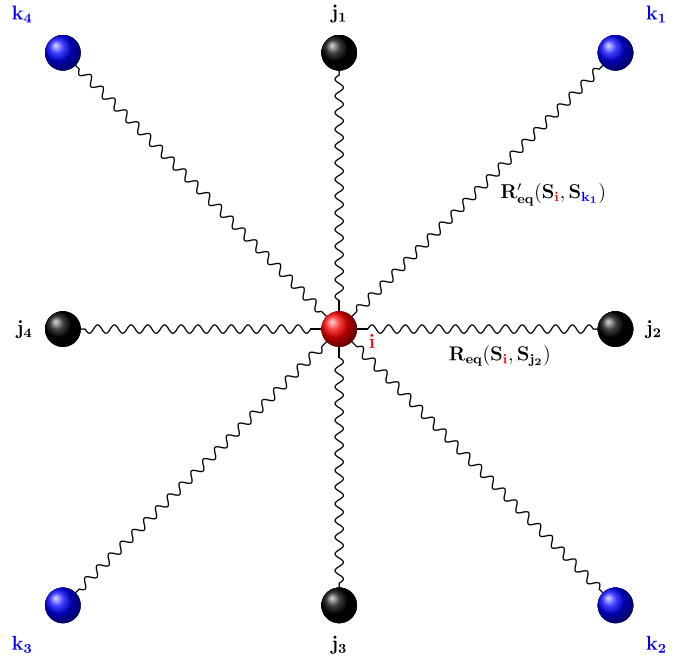

FIG. 1. Lattice configuration showing the atomic links between a site i (red ball) connected to black and blue balls, representing the NN and NNN sites, respectively. The equilibrium bond length between NN (NNN) SCO sites is $R_{eq}(S_i, S_j)$ [$R'_{eq}(S_i, S_j)$].

Since the elastic constant and equilibrium distances between lattice sites depend on the connected spin-state values, the model is described by the following Hamiltonian:

$$H = H_{\text{elec}} + H_{\text{magn}} + H_{\text{elas}}, \tag{1}$$

where H_{elec} stands for the electronic contribution of ligand-field energy which is set to the value $\Delta = 450$ K, and entropy contribution $k_B T \ln(g)$ which stabilizes the HS state [47,49,77–80]:

$$H_{\text{elec}} = (\Delta - k_B T \ln g) \sum_i S_i^2. \tag{2}$$

Within these values of ligand-field and degeneracy ratio, the effective ligand-field energy cancels for the temperature value $T \simeq 90$ K which has the same order of magnitude of the transition temperature of SCO materials.

H_{magn} is the magnetic interaction between the spin states which is only between HS species:

$$H_{\text{magn}} = -\sum_{\langle i,j \rangle} J(r_{ij}) S_i S_j, \tag{3}$$

and H_{elas} denotes the elastic part:

$$H_{\text{elas}} = \frac{1}{2} \sum_{\langle i,j \rangle} A_{ij}(r_{ij}) [r_{ij} - R_{eq}(S_i, S_j)]^2$$
$$+ \frac{1}{2} \sum_{\langle i,k \rangle} B_{ik}(r_{ik}) [r_{ik} - R'_{eq}(S_i, S_k)]^2, \tag{4}$$

which accounts for nearest-neighbor (NN) and next-nearest-neighbor (NNN) interactions between the sites. The NNN interactions are introduced here to maintain the lattice stability

with respect to shear distortion [50–53] particularly during the volume expansion or contraction accompanying the spin transition along the transformation from the LS to HS phases or HS to LS phases. To take into account for the anharmonic effects of the lattice, leading to normal thermal expansion in the LS and HS phases, as well as for the difference of rigidity between the HS and LS phases (HS is less rigid than LS), the respective NN and NNN elastic constants A_{ij} and B_{ik} are written under the following forms:

$$A_{ij}(r_{ij}) = A_0 + A_1(r_{ij} - R_{eq}^{HH})^2 \quad \text{and}$$

$$B_{ik}(r_{ik}) = B_0 + B_1(r_{ik} - \sqrt{2}R_{eq}^{HH})^2, \quad (5)$$

where $\langle i, j \rangle$ and $\langle i, k \rangle$, respectively, run over the NN and NNN bonds, and R_{eq}^{HH} (respectively $\sqrt{2}R_{eq}^{HH}$) is the equilibrium lattice NN (respectively NNN) bond length in the HS state. Thus, denoting by R_{eq}^{LL} (respectively $\sqrt{2}R_{eq}^{LL}$) the NN (respectively NNN) LS equilibrium bond length, we clearly see from Eq. (5) that the NN (respectively NNN) elastic constant in the HS phase is $A_{HH} = A_0$ (respectively $B_{HH} = B_0$), while that of the LS state is $A_{LL} = A_0 + A_1(R_{eq}^{HH} - R_{eq}^{LL})^2 > A_{HH}$ [respectively $B_{LL} = B_0 + 2B_1(R_{eq}^{HH} - R_{eq}^{LL})^2 > B_{HH}$], which meets the constraints of rigidities imposed to two states. However, it is hard to connect a 2D model system to a three-dimensional (3D) material. Indeed, some of the parameters like the ligand field and the degeneracy have been chosen from the experiments. The ligand field Δ corresponds to the enthalpy change at the transition between the LS and the HS state, while the degeneracy ratio $g = g_{HS}/g_{LS}$ connects to the entropy change at the transition through the relation $\Delta S = R \ln(g)$. This quantity is derived from calorimetric measurements, as stated above. For the other parameters, like elastic constants, magnetic interactions, it is really hard to connect them to experimental data, which result from 3D systems, in which in addition anisotropic effects may take place, while here we treat the case of an isotropic 2D system. Furthermore, at least the connection between the bulk modulus Y at 3D and the elastic constants in 2D can be approximated as $Y \simeq A/a$, where A is the elastic constant of the 2D system and a is the lattice parameter. For the other parameters (NNN elastic constant) we do not have any experimental indication, and the strength of the magnetic interactions between the spins' subsystem is taken here as a variable parameter allowing to tune the physical properties of the system.

In the magnetic part of Hamiltonian (1), whose expression is defined in Eq. (3), the exchange term $J(r_{ij})$ represents the local magnetic coupling interaction between NN SCO sites and is written in the form

$$J(r_{ij}) = J_0 - \alpha(r_{ij} - R_{eq}^{HH}), \quad (6)$$

in view to decrease the magnetic interaction during the lattice expansion. In Eq. (6), J_0 and α parameters are taken positive, so as to ensure ferromagnetic interactions between the SCO sites. As a result, the magnetic interaction in a lattice having the lattice parameter of the LS state is $J(r_{ij} = R_{eq}^{LL}) = J_0 + \alpha(R_{eq}^{HH} - R_{eq}^{LL})$, while it is equal to $J(r_{ij} = R_{eq}^{HH}) = J_0$ in the elastic HS phase. This point is important and will be discussed later when we examine the relaxation of photoinduced HS states.

Let us come back to the elastic part of the Hamiltonian (1) defined by Eq. (4) and discuss in more details the involved physical parameters. As stated above, the elastic constants $A_{ij}(r_{ij})$ and $B_{ik}(r_{ik})$ correspond, respectively, to the NN and NNN bond stiffness constants whereas $r_{ij} = \|\vec{r}_i - \vec{r}_j\|$ (r_{ik}) is the instantaneous distance between NN (NNN) i and j $(i$ and $k)$ sites. As it emerges from Eq. (5), bond stiffness constants are taken as parabolic decreasing functions of the instantaneous distances, which then lead to quartic potentials. However, one may easily imagine other types of potentials [81,82] satisfying the experimental condition of soft HS state and rigid LS state. Here, A_0 (B_0) and $A_1 > 0$ $(B_1 > 0)$ are, respectively, the NN (NNN) harmonic and anharmonic contributions to the elastic energy.

The quantity $R_{eq}(S_i, S_j)$ $[R'_{eq}(S_i, S_k)]$ is the equilibrium distance between two NN (NNN) sites i and j $(i$ and $k)$, depending on the connected spin state. Since the spin configuration of two bounded sites can be HS-HS, HS-LS, or LS-LS, we denote their corresponding bond lengths as R_{eq}^{HH}, $R_{eq}^{HL} = R_{eq}^{LH}$ or R_{eq}^{LL}, respectively. Thus, we obtain the following relations: $R_{eq}(+1, +1) = R_{eq}(-1, -1) = R_{eq}(+1, -1) = R_{eq}(-1, +1) = R_{eq}^{HH}$, $R_{eq}(+1, 0) = R_{eq}(0, +1) = R_{eq}(-1, 0) = R_{eq}(0, -1) = R_{eq}^{HL}$, and $R_{eq}(0, 0) = R_{eq}^{LL}$. Due to the square symmetry of the lattice, the equilibrium distances $R'_{eq}(S_i, S_k)$ between NNN sites have been taken equal to those of NN sites multiplied by $\sqrt{2}$. According to these relations, it is straightforward to demonstrate that the spin dependence of the NN distance $R_{eq}(S_i, S_j)$ can be obtained in a unique way as follows:

$$R_{eq}(S_i, S_j) = R_0 + 2R_1(S_i^2 + S_j^2) + R_2 S_i^2 S_j^2, \quad (7)$$

where $R_0 = R_{eq}^{LL}$, $R_1 = \frac{1}{4}(R_{eq}^{HH} - R_{eq}^{LL})$, and $R_2 = R_{eq}^{HH} + R_{eq}^{LL} - 2R_{eq}^{HL}$. Evidently, the R_0 represents the NN LS equilibrium distance, while R_1 corresponds to the misfit of lattice parameter between the HS and LS states, and $R_2 = 2(\frac{R_{eq}^{HH} + R_{eq}^{LL}}{2} - R_{eq}^{HL})$ represents the difference between the center of mass of HS and LS lattice parameter and that of HS-LS configuration. In this work, we take for simplicity $R_{eq}^{HL} = \frac{1}{2}(R_{eq}^{HH} + R_{eq}^{LL})$, which then gives $R_2 = 0$.

A preliminary analytical examination of the role of the bond stiffness in the energetic stabilization of the spin states helps in the understanding of the relevant parameters controlling the thermodynamic properties of this electroelastic Hamiltonian. For that, we limit ourselves to the case of negligible NNN interaction and negligible anharmonic contributions. Using Eq. (7), Hamiltonian (1) is reexpressed in terms of the BEG Hamiltonian

$$H = -\sum_{\langle i,j \rangle} J(r_{ij})S_i S_j + \sum_{\langle i,j \rangle} K(r_{ij})S_i^2 S_j^2 \\ + \sum_i D_i S_i^2 + \frac{A_0}{2} \sum_{\langle i,j \rangle} (r_{ij} - R_0)^2, \quad (8)$$

where the parameters $J(r_{ij})$, $K(r_{ij})$, and D_i are the local magnetic coupling interaction, the local quadrupolar interaction, and the local crystal-field contributions, respectively. The two first interaction parameters are given by

$$J(r_{ij}) = J_0 - \alpha(r_{ij} - R_{eq}^{HH}) \quad \text{and} \quad K(r_{ij}) = 4A_0 R_1^2, \quad (9)$$

and the effective local crystal field writes

$$D_i = \Delta - k_B T \ \ln(g) + 2A_0 R_1 \left[zR_1 - \sum_{j=1}^{z} \left(r_{ij} - R_{eq}^{LL} \right) \right]. \tag{10}$$

The fact that the quadrupolar interaction K, which is here positive and exclusively short range, indicates that this term stabilizes NN spin configurations $S_i = 0$, $S_j = \pm 1$ or $S_i = 0$, $S_j = 0$ which means HS-LS or LS-LS configurations. In contrast, the magnetic term stabilizes HS-HS (i.e., ± 1- ± 1) neighboring sites. On the other hand, the effective crystal field acting on a spin site now depends on the elastic field created by the neighbors which acts as an internal pressure. The inspection of the elastic contribution $2A_0 R_1 [zR_1 - \sum_{j=1}^{z}(r_{ij} - R_{eq}^{LL})]$ to the effective crystal field shows that it is positive when $r_{ij} = R_{eq}^{LL}$ (LS bond length) thus stabilizing the LS state and becomes negative for $r_{ij} = R_{eq}^{HH}$ (HS bond length) stabilizing the HS state. This behavior of the elastic field establishes a direct synergy between the entropic effects of the degeneracy and the elastic interactions.

III. TWO-STEP MONTE CARLO ALGORITHM

A planar lattice of square symmetry with $N = L_x \times L_y$ SCO sites is considered with free boundary conditions. The simulations are alternatively executed on spin and position variables in a two-step strategy. The metropolis algorithm is considered for the spins' and lattice positions' update procedure (sites' displacements). Then, the stochastic algorithm is performed in the following way: for a site (i, j) randomly selected, with spin $S_{ij} = \pm 1, 0$ and position r_{ij}, a new spin value S'_{ij} [such that $S_{ij} \rightarrow S'_{ij} = \pm 1, 0$ $(S_{ij} \neq S'_{ij})$] is set without position change. This spin change is accepted or rejected by the usual Metropolis criterion. Whatever the result (acceptance or rejection), the lattice whole is relaxed mechanically by a slight motion of nodes (selected randomly) with a quantity $\delta u = 0.03$ (in any direction: $u = x, y$) which is much smaller than the distance between the spin states. The lattice relaxation is also performed following a Monte Carlo technique at fixed spin configuration. The procedure of the lattice relaxation is once repeated for each spin flip. Afterwards, a new spin site will be selected randomly and so on, etc. Once all nodes of the lattice are visited for the spin change, we define such step as the unit of the Monte Carlo step and denote it "MCS." Physical quantities of interest are calculated in the steady state with $N_S = 10^5$ MC steps per site for the spin-flip dynamics and for each spin-flip attempt, all SCO unit displacements are once attempted (one Monte Carlo cycle). Specifically, a spin variable and its position are randomly selected within the possible projections with a uniform distribution. About $N_E = 2 \times 10^4$ MC steps per site are considered for thermal equilibration in the spin-flip dynamics and then discarded from the averaging procedure. Three to five independent runs are performed on each MC process in view to get smooth data. The lattice magnetization is calculated as follows:

$$m = \langle S \rangle = \frac{1}{N} \sum_{i=1}^{N} S_i. \tag{11}$$

The n_{HS} fraction is evaluated as follows:

$$n_{HS} = \langle S^2 \rangle = \frac{1}{N}(N_+ + N_-), \tag{12}$$

where N_+ and N_- are numbers of spins in the up and down states, respectively. The magnetic critical temperature T_C is defined in this work as the temperature associated to the peak in the magnetic susceptibility curve when the magnetization is continuously decreasing to vanish. The magnetic susceptibility is calculated by the formula

$$\chi = \langle \langle (\overline{S})^2 \rangle - m^2 \rangle, \tag{13}$$

where $\overline{S}$ is the averaged system magnetization at a given step of the simulation and $\langle \ldots \rangle$ denotes a statistical average over the $(N_S - N_E)$ MC steps. Another transition temperature of interest $T_{1/2}$ is that of the spin-transition phenomenon which occurs when the HS fraction n_{HS} is equal to $\frac{1}{2}$. We also calculate the average intermolecular distance $\langle d \rangle$ between NN SCO sites that provides information about the lattice "volume" change along the spin transition. Its expression is given by

$$\langle d \rangle = \frac{\sum_{\langle i, j \rangle} \sqrt{(x_j - x_i)^2 + (y_j - y_i)^2}}{(L_x - 1)L_y + (L_y - 1)L_x}, \tag{14}$$

with i and j run $[1, L_x]$ and $[1, L_y]$ respectively.

IV. RESULTS AND DISCUSSIONS

This work uses as far as possible realistic model parameters values, already derived in previous electroelastic modeling of SCO materials by one of the authors [50–56]. The chosen ligand-field energy value $\Delta = 450$ K leads to a molar enthalpy variation at the transition $\Delta H \simeq 3.7$ kJ mol^{-1}, while the entropy change at the transition, already evaluated to $\Delta S \simeq 41.7$ J K^{-1} mol^{-1}, gives a spin-transition temperature $T_{1/2} = \frac{\Delta H}{\Delta S} = \frac{\Delta}{k_B \ln g} \simeq 90$ K.

As well, the values of equilibrium distances between two NN sites, which depend on the spin configuration of linked sites, are taken as follows: $R_{eq}^{HH} = 1.2$ nm, $R_{eq}^{LL} = 1$ nm, $R_{eq}^{HL} = \frac{1}{2}(R_{eq}^{HH} + R_{eq}^{LL}) = 1.1$ nm. In view of the square 2D symmetry of the lattice, the NNN equilibrium distances are simply chosen as $R_{eq}'^{HH} = \sqrt{2}R_{eq}^{HH}$, $R_{eq}'^{LL} = \sqrt{2}R_{eq}^{LL}$, and $R_{eq}'^{HL} = \sqrt{2}R_{eq}^{HL}$ for the three possible electronic configurations. It is worth mentioning that the value of the lattice misfit ($R_{eq}^{HH} - R_{eq}^{LL}$) is taken a little bit high in order to enhance the lattice distortions for the small lattice sizes, investigated in this study.

The effect of the elastic intermolecular interactions on the SCO transition is investigated by considering different values of the elastic constants. Indeed, the variation of the equilibrium intermolecular distance and bond stiffness upon the LS to HS transition results in volume and bulk modulus changes, which are experimental features of the spin transition in SCO solids [83–89]. Here, we take $A_0 = B_0$ in the range 500 to 10^4 K nm^{-2}, leading to an order of magnitude of bulk modulus $E \simeq A_0/R_{eq}$ in the range 0.1–2 GPa, in quite good agreement with bulk modulus of polymeric materials. The anharmonic contributions to the elastic constants are, for simplicity, taken as $A_1 = B_1 = 10A_0$. However, it is important to notice that their contributions $A_1(r_{ij} - R_{eq}^{HH})^2$ to the total

elastic stiffness are maximum in the LS state and are equal to $A_1(R_{eq}^{LL} - R_{eq}^{HH})^2 = 200$ K (for $A_0 = 500$ K nm^{-2}) which then represents 40% of the total elastic energy.

Another contribution with respect to previously published electroelastic models concerns the magnetic interaction between the SCO units, represented in Hamiltonian (3) by the local exchange interaction $J(r_{ij})$. The values of the constant part J_0 of this term are selected in the range $J_0 = 30$–100 K, which leads in a simple Onsager 2D model lattice to magnetic transition temperatures in the range 85–226.90 K. The parameter α, representing the magnetoelastic coupling in this model, is taken in the range of $\alpha = 0$–700 K nm^{-1} values. The total magnetic energy reaches its maximum value, when all spin states are LS and lattice bond lengths are equal to those of the LS lattice ($r_{ij} = R_{eq}^{LL}$). In this case, the magnetoelastic contribution exchange interaction $J = J_0 - \alpha(r_{ij} - R_{eq}^{HH})$ takes its maximum value 20 K which still remains small compared to J_0 for $J_0 = 50$ K and $\alpha = 100$ K nm^{-1}.

A. Finite-size effects in gradual spin and magnetic transitions

The application of the two-step MC procedure enables us to estimate steady-state finite-size effects on various physical quantities, namely the HS fraction n_{HS}, the net magnetization m, the magnetic susceptibility χ, and the average intermolecular distance $\langle d \rangle$ between NN SCO sites, as well as spin-spin correlation C. Various system sizes 8×8, 12×12, 16×16, and 16×24 SCO units are selected and investigated. Corresponding numerical results are illustrated in Fig. 2. The simulations are performed with the value of the NN harmonic elastic interaction $A_0 = 2000$ K nm^{-2}, for which we do not expect a first-order spin transition, but rather a continuous transformation from LS to HS.

In Fig. 2(a), the temperature dependence of the HS fraction n_{HS} is presented for different system sizes. The set of obtained curves shows a continuous gradual transition between the values $n_{HS} = \langle S^2 \rangle = 0$ (LS state) and $n_{HS} = 1$ (HS state). It evidently appears that finite-size effects are almost negligible for lattice sizes beyond 16×16. Figure 2(b) displays the net magnetization m, which shows a reentrantlike behavior. Indeed, m is zero in the temperature interval 0–50 K and then suddenly increases, goes through a maximum, the height of which increases with system size, and finally falls down at high temperatures, i.e., in the HS phase. The final value of m decreases as the system's size increases, indicating that in the thermodynamic limit this value will be zero, and the system will reach the paramagnetic phase. These observations ensure that in the thermodynamic limit, the magnetization will reach its maximum value, not necessarily, $m = 1$, and its nonzero value will only prevail in a narrow temperature range. These observations suggest that at low and high temperatures, the system will be globally nonmagnetic. Indeed, at low temperatures, the LS state ($\langle S^2 \rangle = 0$ and $\langle S \rangle = 0$) is stabilized by the ligand-field and the elastic interactions, and so one gets $m = 0$ and $n_{HS} = 0$. This is a strictly diamagnetic phase, where the SCO lattice is exclusively populated by spins of values 0. In the high-temperature limit, the states $S = +1$ and -1 are equally populated, and the HS sate is favored, which leads to stabilize the paramagnetic state characterized by $m = 0$ and $n_{HS} = 1$ for very large systems. Between the
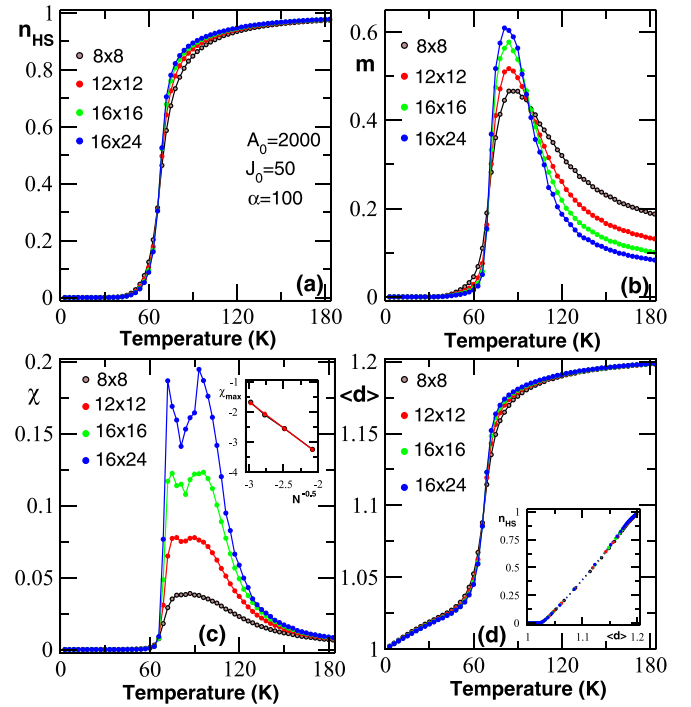

FIG. 2. Thermal behavior of (a) HS fraction n_{HS}, (b) magnetization m, (c) magnetic susceptibility χ, and (d) average intermolecular distance $\langle d \rangle$ between NN SCO molecules, for four system sizes: 8×8, 12×12, 16×16, and 16×24 showing the finite-size effects on the model. Inset in (c) represents $\log(\chi_{max})$ as function of $\log(N^{-0.5})$ (black curve), and its corresponding linear regression (red curve). χ_{max} denotes the first peak height of χ and N is the total number of SCO sites. Inset in (d) illustrates the correlation between n_{HS} and $\langle d \rangle$ for different system sizes considered, when temperature increases. The used parameters for all panels are $A_0 = 2 \times 10^3$ K nm^{-2}, $J_0 = 50$ K, $\alpha = 100$ K nm^{-1}, $\Delta = 450$ K, and $g = 150$.

two previous phases, a totally or partially ordered phase with $m \neq 0$ and $n_{HS} \neq 0$ emerges [see Figs. 2(a) and 2(b)]. Here, a ferromagnetic phase appears embedded in two nonmagnetic phases. The above observations are strengthened by the computation of the magnetic susceptibility curves, illustrated in Fig. 2(c). Two peaks can be observed for each system, except for the low-sized one. The first peak appears after a very sharp jump of $\chi(T)$ and is attributed to the spin transition which occurs at about $T = 72$ K for the 16×24 system. A direct finite-size analysis of the behavior of the first peak height χ_{max} with system size formally given by the square root of the system volume (number of SCO units) is performed [see inset of Fig. 2(c)]. Calculations yield a behavior of the form $\chi_{max} \simeq N^{0.5\delta}$. The extracted exponent from a log-log plot is $\delta = 1.75 \pm 0.06$, which value is close to the 2D system. This scaling result physically indicates that the peak is associated to a macroscopic instability in the system that results from microscopic cooperative phenomena to which most SCO units contribute. This instability is of first-order kind and is accompanied by a hysteresis phenomenon. The associated pseudotransition temperature is slowly decreasing with increasing system size showing some convergence. It is important to mention that the critical exponent is "measured" on the magnetic subsystem which is, of course, coupled to
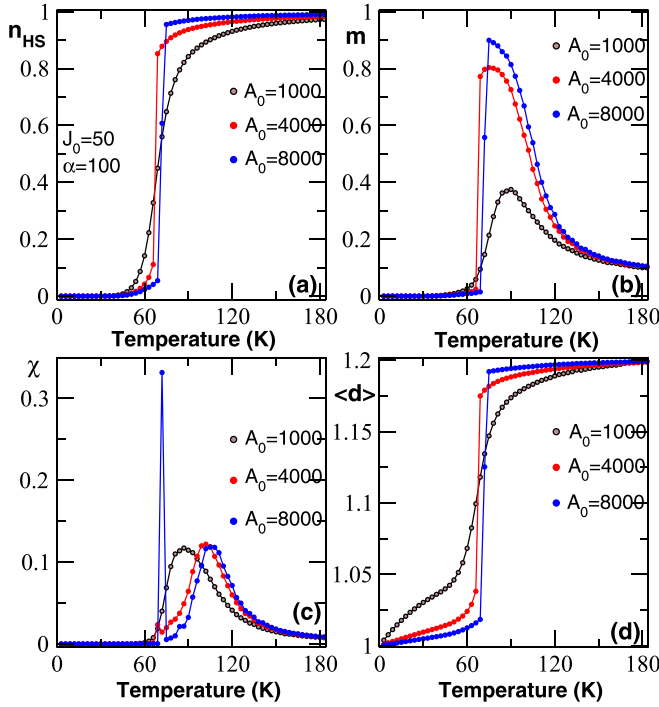
FIG. 3. Some thermal behaviors of the model for 16×16 system and varying the values of the elastic constant A_0 with fixed other parameters. (a) HS fraction n_{HS}, (b) magnetization m, (c) magnetic susceptibility χ, and (d) average intermolecular distance $\langle d \rangle$ between NN SCO molecules. The curves show that one moves from a continuous behavior to the appearance of discontinuities, which are first-order transitions, when A_0 increases. For large values of A_0, the magnetic susceptibility χ presents two peaks, where the first one corresponds to the first-order spin transition, and the second one is attributed to the order-disorder transition. For all panels, other values of used parameters are $J_0 = 50$ K, $\alpha = 100$ K nm^{-1}, $\Delta = 450$ K, and $g = 150$.

the SCO elastic lattice through the magnetoelastic interaction. However, the effect of the SCO transition is to drive the system from the diamagnetic ($S = 0$) to magnetic state ($S^2 = +1$) through first-order or gradual transformation (Figs. 2 and 3). But then, when the magnetic order is generated, the SCO elastic interactions play a negligible role in the system's behavior (the lattice parameter becomes almost that of the HS and does not change a lot). As a result, the magnetic transition from the ferromagnetic to the paramagnetic state, which takes place at higher temperature than the SCO transition, mainly follows the behavior of that of an Ising model, although the "exchange" interaction J slightly depends on the distances as $J(r_{ij}) = J_0 - \alpha(r_{ij} - R_{eq}^{HH})$. However, as we explained above, in the HS region, one has $\langle r_{ij} \rangle \simeq R_{eq}^{HH}$, and so the effect of the long-range interactions on the magnetic subsystem remains negligible. That is the main reason for which the same critical exponent as that of the 2D Ising model is found in these simulations.

The second less sharp peak is attributed to a second-order phase transition taking place in the HS state between the ferromagnetic phase at intermediate temperatures and the paramagnetic disordered phase that prevails at high temperature. For the 16×24 system, the ferromagnetic phase exists

between temperatures associated to both peaks of χ which are estimated to 72 and 93 K. The order-disorder transition temperature $T_C \simeq 93$ K well corresponds to the expected Onsager critical temperature of a 2D Ising system $T_C = 2.269[J_0 - \alpha(\langle d \rangle - R_{eq}^{HH})]$. Using these values, the critical temperature is estimated using Onsager formula $T_{Ons} = 2J/\ln(1 + \sqrt{2})$ which gives $T_{Ons} = 2.269J_0 = 113.4$ K in the case of a perfect HS system, for $J_0 = 50$ K. On the other hand, at the maximum value of χ, the corresponding HS fraction value is $n_{HS} \simeq 0.9$ (the magnetization peaks at $m \simeq 0.6$) indicating that the present ferromagnetic phase is only partially ordered. Consequently, the ferromagnetic phase of Fig. 2(b) must be seen as a diluted phase containing about 10% of diamagnetic LS phase, randomly distributed. Thus, the critical transition temperature is lower than that of the pure saturated HS phase and can be estimated in a simple attempt as $T_{Ons}^{dilut} = 0.9T_{Ons} \simeq 103$ K. It is, however, important to mention that the ferroparamagnetic transition temperatures, estimated from the MC simulations, crucially depends on the system size. Thus, for a finite system, the critical temperature is always lower than that of Onsager, to which it connects through the relation $T_C = T_{Ons}/(1 + \frac{5}{4\sqrt{N}})$ [90], where N is the system "volume." According to these developments, one can evaluate analytically using, for the case 16×16 system, the expected ferromagnetic to paramagnetic transition temperature as $T_C = T_{Ons}^{dilut}/(1 + \frac{5}{4\sqrt{N}}) \simeq 95$ K, which is in excellent agreement with the value $T_C = 93$ K emerging from the simulations.

One crucial parameter of the model is the average intermolecular distance $\langle d \rangle$ between NN SCO molecules. Reported in Fig. 2(d), its behavior with temperature is quite similar to that of n_{HS} and finite-size effects are also found negligible on this quantity beyond the 16×16 system size. The linear increase of intermolecular distance $\langle d \rangle$ in the HS and LS phases is due to thermal expansion, caused by the anharmonic (quartic) elastic term of the Hamiltonian. Due to the form of the anharmonic contribution $[A_1(r_{ij} - R_{eq}^{HH})^2]$ to the NN elastic constant, which is stronger in the LS spin state ($r_{ij} = R_{eq}^{LL}$) and almost negligible in the HS state ($r_{ij} = R_{eq}^{HH}$), the slope of the curve $\langle d \rangle(T)$ is higher in the LS phase. According to this behavior, the thermal expansion coefficient for the NN bond length, defined as $\alpha_T = d(\ln\langle d \rangle)/dT$, leads to the value, 6.4×10^{-4} K^{-1}, which is found the same for all investigated system sizes. This value strongly depends of the anharmonic elastic constant A_1 which was taken quite high in the simulations ($A_1 = 10A_0$) in order to magnify this phenomenon. In the temperature interval 60–90 K, the intermolecular distance, undergoes a rapid increase in the same region of first-order transition as that of the HS fraction [see Fig. 2(a)] and finally saturates at high temperatures. This thermal behavior of $\langle d \rangle$ leads to an important remark concerning the magnetic properties. Indeed, the total exchangelike interaction J depends on the NN distance between the SCO sites, and therefore at fixed temperature T, its average value $\langle J \rangle = J_0 - \alpha(\langle d \rangle - R_{eq}^{HH})$ is clearly temperature dependent. This makes the study of the magnetic subsystem more complex than thought, and in the same time this fact makes the problem extremely close to the previous BEG studies [47,78–80] in which all interacting parameters, including magnetic exchange, were assumed to be linearly dependent on temperature.

The fact that a sharp transition takes place exactly in the same region for the electronic state, that is the HS fraction parameter [see Fig. 2(a)], and the structure, that is the lattice parameter, is a key MC result of the model which reproduces experimental observations on SCO solids at the spin transition. The correlation between n_{HS} and $\langle d \rangle$ is also explored by computing n_{HS} as function of $\langle d \rangle$ [see inset of Fig. 2(d)] as the temperature varies. Corresponding data collapse for different system sizes in a straight line of slope 0.2 nm, establishing an undoubtedly evident correlation between n_{HS} and $\langle d \rangle$. The thermal behavior of the spin-spin correlation function $C(T) = \langle S_i S_j \rangle$ has been also examined with system size. The results (not reported) are similar to those observed in Fig. 2(b). Fewer finite-size effects are obtained at low and high temperatures than in Fig. 2(a). In these temperature ranges, curves for different system sizes collapse.

B. Effect of the harmonic elastic constant A_0

Now, we study the effect of the model parameter values on the system. For that, since large-scale computing properties of the model are demanding in simulation time, the 16×16 system is selected to predict qualitatively the thermal behavior of magnetization m, HS fraction n_{HS}, magnetic susceptibility χ, and average intermolecular distance $\langle d \rangle$, as function of the elastic constant A_0. Figure 3 summarizes the system's behavior for three values of this constant: $A_0 = 1000$, 4000, and 8000 K nm^{-2}. One sees that the HS fraction n_{HS} [see Fig. 3(a)] changes from gradual to sharp discontinuous transition with unchanged transition temperature $T_{1/2} \sim 69$ K. This behavior can be well understood since the transition temperature between the LS and HS states involves only a change of the total effective ligand field, whose elastic part vanishes at the transition. Therefore, the transition temperature at which the system switches between the LS and HS states only depends on Δ, J_0, and g. Figures 3(b) and 3(c) show the magnetization m and the susceptibility χ which also change from a continuous transition character to discontinuous when values of the elastic constant A_0 increases. Thus, for $A_0 = 4000$ and 8000 K nm^{-2}, the magnetization jumps from 0 to 0.9 exactly at the SCO transition and then vanishes following a second order-disorder transition whose critical temperature T_C depends on A_0, as well indicated by the shift of the broad maxima of the susceptibility χ [see Fig. 3(c)]. This behavior highlights the effect of the elasticity of the material on the magnetic properties. Finally, Fig. 3(d) shows that the average intermolecular distance $\langle d \rangle$ is influenced by the change of A_0 mainly in the LS state where the LS lattice distance $\langle d \rangle = 1$ nm is stabilized for high A_0 while the transition transforms from gradual to first order, in agreement with $n_{HS}(T)$ behavior.

C. Effects of the magnetic coupling J_0 and the magnetoelastic coupling constant α

As for Fig. 3, quite similar tendencies are observed for increasing values of the coupling constant J_0 at fixed A_0 value (see Fig. 4). However, one can remark the existence of notable differences between the effects of A_0 and J_0. First of all, increasing J_0 from 30 to 100 K shifts downward the spin-transition temperature, as indicated in Fig. 4(a), and so
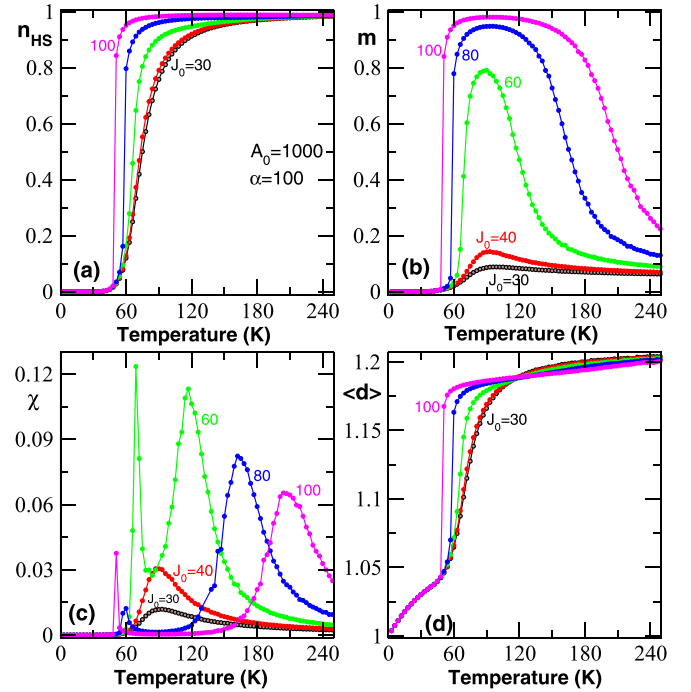

FIG. 4. Some thermal behaviors of the model for 16×16 system and varying magnetic coupling interaction J_0 with fixed other parameters. (a) HS fraction n_{HS}, (b) magnetization m, (c) magnetic susceptibility χ, and (d) average intermolecular distance $\langle d \rangle$ between NN SCO molecules. Second- and first-order transitions are obtained for selected values of J_0, and the curves shift to low temperatures by increasing J_0 values as obtained in ours previous works [78,79]. Two peaks appear in the magnetic susceptibility behavior at high values of J_0, whereas only one is depicted for its low values [see (c)]. For all panels, other values of considered model parameters are $A_0 = 10^3$ K nm^{-2}, $\alpha = 100$ K nm^{-1}, $\Delta = 450$ K, and $g = 150$.

the exchange coupling J_0 stabilizes the magnetic HS spin phase while giving a sharper character to the spin transition, as A_0 does. It is interesting to notice that the SCO transition temperature can be determined analytically in this model. At the switching temperature between the LS and HS states, free energies of HS and LS phases must be equal. Let us denote by P_{HS} and P_{LS} the probabilities of occupying HS and LS sites, respectively. Their general expressions are given as $P_{HS} = \Omega_{HS} e^{-\beta E_{HS}}$ and $P_{LS} = \Omega_{LS} e^{-\beta E_{LS}}$, where Ω is the electronic degeneracy of the spin state ($\Omega_{HS} = 2$ and $\Omega_{LS} = 1$) and E_{HS} (respectively E_{LS}) is the energy per site in the HS (respectively LS) state. At the transition, one has $P_{HS} = P_{LS}$. On the other hand, the transition takes place between LS and HS ordered phases (their mixing entropies are equal to zero). Moreover, the elastic energies of HS and LS phases are also zero [see Eq. (4)] and, therefore, the energies of the HS and LS phases are simply given by $E_{HS} = D_{eff} - J_0$ [where $D_{eff} = \Delta - k_B T \ln(g)$] and $E_{LS} = 0$, respectively. At the transition we then have $e^{-\beta[(\Delta - k_B T_{1/2} \ln 2g) - J_0]} = 1$, which leads to the transition temperature $k_B T_{1/2} \simeq \frac{\Delta - J_0}{\ln 2g} = 72$ K for $J_0 = 40$ K, which is in excellent agreement with that of MC simulations, derived from Fig. 4(a) for $n_{HS} = \frac{1}{2}$: when a half of the system has switched from the LS to the HS state.

In this problem, the system exhibits two magnetic transitions. The first one, strongly correlated to the SCO transition, takes place between the diamagnetic state ($\langle S^2 \rangle = 0$ and ferromagnetic state ($\langle S^2 \rangle = 1$). The second ferromagnetic-paramagnetic order-disorder transition takes place at higher temperature in the present studied cases. To observe a crossover between the critical exponent of 2D Ising model and that of mean-field universality class, we must have a long-range magnetic coupling between the spin states along the ferromagnetic to paramagnetic transition. In other words, there must be a strong interference between the magnetic transition temperature and the SCO temperature. If these two temperatures are very close, then the two transitions will interfere and as a result the magnetic interaction $J(r_{ij})$ will strongly depend on the lattice parameter in the temperature region where the magnetic phase transition takes place between the ferromagnetic and the paramagnetic HS states. Although interesting, we believe that this type of study merits a specific work.

The shift of the SCO transition can be evaluated through the relation $T_{1/2} = \frac{\Delta - J_0}{k_B \ln 2g}$ in the domain where the second-order and SCO-transition temperatures are very close regarding to J_0 values (e.g., for $J_0 = 30$ K, $T_c = 90$ K, and $T_{1/2} = 75$ K with MC simulations) and the exact relation yields $T_{1/2} = 73.63$ K. This estimation is in fair agreement with the MC simulations of Figs. 4(a) and 4(b). Beyond that, the obtained result leads to a lowering of the first-order transition temperatures ($T_{1/2} = 52$ K for MC simulations) by of 61.36 K and with $T_c = 204$ K, for high second-order transition temperature, when J_0 is increased to 100 K. As such, this leads to having nonvalid relation between $T_{1/2}$ and $\frac{\Delta - J_0}{k_B \ln 2g}$. This effect is also found in the magnetic transition [see Fig. 4(c)], which also shows a huge effect of J_0 on the second-order phase transition, as expected from theory of 2D Ising systems. Indeed, a clear saturation of the magnetization m at high temperatures and an increasing of the domain of the ferromagnetic phase with J_0 which is a common feature in Ising systems [49,77,78]. Here, the HS units are created and interact magnetically in the system. Overall, in Fig. 3 we demonstrated that a strong enough harmonic elastic coupling A_0, induced a first-order SCO [on $n_{HS}(T)$], and triggered a first-order transition on the magnetization $m(T)$ from the LS diamagnetic state to an ordered (or partially ordered) ferromagnetic state. Here, we also demonstrate that the opposite effect is also possible since an increasing magnetic interaction J_0 induces a first-order SCO transition. This interplay between the elastic and the magnetic interactions is even more flagrant in the curves of Fig. 4(d), which present significant effect of J_0 on the average intermolecular distance $\langle d \rangle$, which is a purely structural quantity. Here, we see that the slopes of $\langle d \rangle(T)$, in the HS phase change with respect to J_0, which means that even the thermal expansion coefficient ($\frac{d \ln \langle d \rangle}{dT}$) depends on J_0 values. This proves that the magnetoelastic interaction introduced in this model is very efficient and allows a strong coupling between the magnetic and the structural properties of the lattice. Thus, the average intermolecular distance $\langle d \rangle$ from the LS diamagnetic state to an ordered (or partially ordered) ferromagnetic state is a relevant parameter that shows the relationship between the
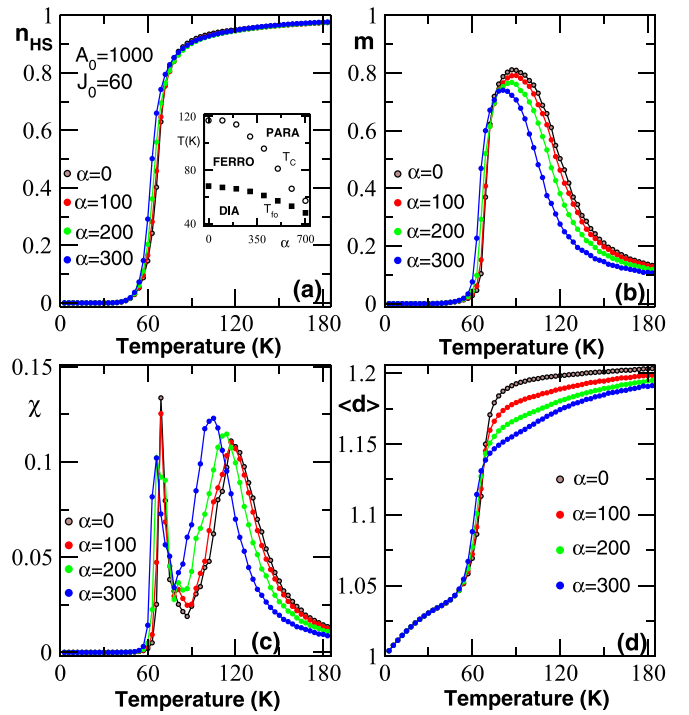

FIG. 5. Some thermal behaviors of the model for 16×16 system and varying the magnetoelastic coupling α with fixed other parameters. (a) HS fraction n_{HS}, with inset that is the corresponding phase diagram, (b) magnetization m, (c) magnetic susceptibility χ, and (d) average intermolecular distance $\langle d \rangle$ between NN SCO molecules. Second- and first-order transitions are obtained, for selected values of α, and the curves shift to low temperatures by increasing α values. Two peaks appear in the magnetic susceptibility behaviors, at any values of α [see (c)]. Diaferromagnetic and ferroparamagnetic phase transitions occurred as displayed the inset phase diagram in (a). For all panels, other values of considered model parameters are $A_0 = 10^3$ K nm^{-2}, $J_0 = 60$ K, $\Delta = 450$ K, and $g = 150$.

system volume change and the magnetoelastic interaction. In addition, as in Fig. 4, similar tendencies are observed for increasing values of the magnetoelastic coupling α at fixed J_0 and A_0 values (see Fig. 5). For increasing α values, one gets first- and second-order transitions where the former coincides to the equilibrium spin-transition temperature ($n_{HS} = \frac{1}{2}$). All transition temperatures shifted to lower values with increasing α value as depicted in the inset of Fig. 5(a). For $J_0 = 60$ K and $A_0 = 1000$ K nm^{-2}, diaferromagnetic and ferroparamagnetic characters of the transition are found from thermal behaviors of the thermodynamic quantities (HS fraction n_{HS}, magnetization m, and magnetic susceptibility χ).

D. Phase diagrams

It should be interesting to devise the temperature phase diagram of the model, relying on the behavior of the HS fraction, and the magnetic susceptibility. The results as functions of A_0 and J_0, for two selected values of J_0 [Figs. 6(a) and 6(b)] and for two selected values of A_0 [Figs. 6(c) and 6(d)], respectively. It is observed that the high-temperature phase is a disordered phase, and the low-temperature one is a diamagnetic phase. The intermediate phase is the ferromagnetic
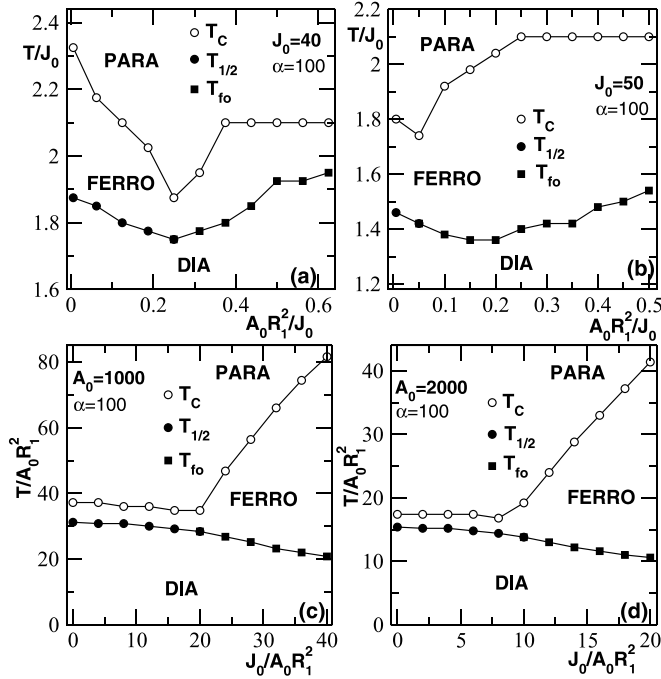
FIG. 6. Thermal phase diagram of the model in the reduced parameters ($A_0 R_1^2/J_0$, T/J_0) and ($J_0/A_0 R_1^2$, $T/A_0 R_1^2$) planes for 16×16 system, with selected values of J_0 [(a) and (b)] and A_0 [(c) and (d)], respectively. Three phases are found: diamagnetic, paramagnetic, and ferromagnetic phases. Lines with solid circular dots (solid square dots) denote the equilibrium temperature $T_{1/2}$ [the first-order spin-transition temperature T_{fo} (first peak of χ)], whereas that with open circular dots are associated to order-disorder transition temperature T_C (second peak of χ). Large domain of ferromagnetic phase appears when the magnetic coupling interaction J_0 increases, and the phase diagram does not show tricritical points anywhere. Other model parameters values are $\alpha = 100$ K nm^{-1}, $\Delta = 450$ K, and $g = 150$.

phase, that is separated from the diamagnetic phase by continuous spin transitions at low values of A_0 (or J_0, respectively), and by first-order transitions at higher values of both parameters. It is important to notice that the model does not exhibit tricritical points for the selected values of J_0 (or A_0, respectively), contrarily to observations done in our previous works, where only spin-flip dynamics are considered. This absence could be a finite-size effect. From Figs. 6(a) and 6(b), it emerges that the transition lines decrease as function of A_0, with the presence of a sharp kink in the T_C lines at $A_0 R_1^2 = 10$ and 2.5 K, respectively, in Figs. 6(a) and 6(b). Beyond these kinks, the spin transition occurs through a first-order transition at low temperatures, where discontinuities are observed in the thermal behaviors of the order parameters. In this range of $A_0 R_1^2$, the transition lines increase and reach their limit values. With increasing J_0 value, one can remark that the domain of the ferromagnetic phase increases as in most Ising-type ferromagnetic systems as previously stated, and the onset temperature for the appearance of the first-order transition decreases. This remark is also observed in Figs. 6(c) and 6(d), where the transition lines decrease slightly when J_0 increases, with appearance of a sharp kink at about $J_0 = 50$ K [Fig. 6(c)] and $J_0 = 40$ K [Fig. 6(d)] in the T_C lines. From these values of J_0, the spin-transition lines are first order, and may decrease
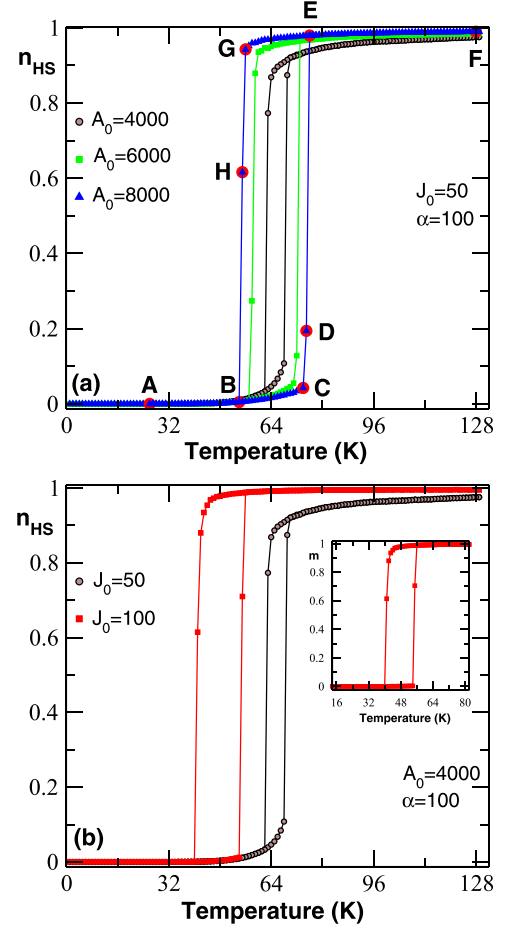

FIG. 7. Thermal hysteresis loop of the HS fraction n_{HS} at the vicinity of first-order transition for selected values of A_0 and J_0, respectively, in (a) and (b). The system size is 32×32. The loop area increases with the elastic constant A_0, where their center is almost fixed in temperature. Whereas, for increasing J_0 values, the loop area increases and shifts to left for low temperatures. The inset in (b) shows thermal hysteresis loop of the magnetization m, for $J_0 = 100$ K. A, B, C, D, E, F, G, and H are the positions of lattice configurations of Fig. 9 on the upward and backward branches, at different temperatures associated, respectively, to $T_1 = 26$ K, $T_2 = 54$ K, $T_3 = 74$ K, $T_4 = 75$ K, $T_5 = 76$ K, $T_6 = 126$ K, $T_7 = 56$ K, and $T_8 = 55$ K. We take $\Delta = 450$ K and $g = 150$ with other model parameters which are written in panels.

with J_0, whereas the T_C lines undergo a rapid increase, resulting in the increase of ferromagnetic phase domain.

E. Thermal hysteresis behaviors of the system

At the vicinity of first-order transitions, hysteresis phenomena are observed. Here a 32×32 system is considered and the calculations are proceeded as follows. The temperature is raised from 1 to 130 K with an increment of 1 K. When 130 K is reached, the simulations continued to 1 K with a temperature step of -1 K. The hysteresis cycles achieved are illustrated in Fig. 7 for varying values of the parameters A_0 [Fig. 7(a)] and J_0 [Fig. 7(b)] and selected values of other parameters that are indicated in the panels. It is observed that when the value of A_0 is raised, the switching temperature of
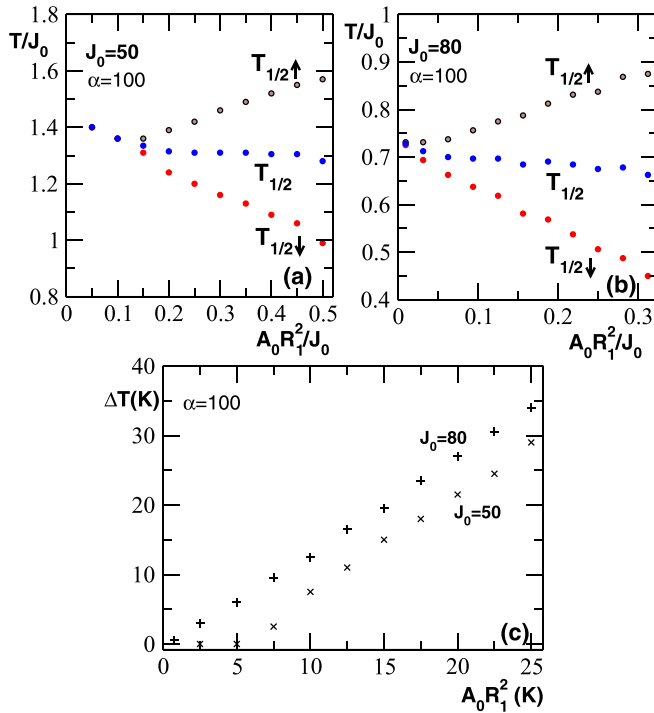
FIG. 8. Phase diagram of 32×32 system, as function of $A_0 R_1^2 / J_0$, showing the dependence of limiting temperatures of hysteresis loops ($T_{1/2\uparrow}$, $T_{1/2\downarrow}$), and the associated equilibrium temperature approximated by $T_{1/2} = (T_{1/2\uparrow} + T_{1/2\downarrow})/2$ for $J_0 = 50$ K (a) and $J_0 = 80$ K (b). The corresponding hysteresis width ΔT is displayed in (c) and shows increasing of loop area with $A_0 R_1^2$. Other values used for model parameters are $\alpha = 100$ K nm^{-1}, $\Delta = 450$ K, and $g = 150$.

the upward branch $T_{1/2\uparrow}$ increases while that of the downward branch $T_{1/2\downarrow}$ decreases [see Fig. 7(a)]. As a consequence, the cycle area increases with A_0. Interestingly, the center of the cycle evidently remains almost constant in this A_0 range, in good agreement with the previous analytical predictions which indicated that the transition temperature at equilibrium does not depend on the harmonic elastic constant A_0. On the contrary, increasing values J_0 shift the hysteresis loop to low temperatures with a decrease of the associated $T_{1/2\uparrow}$ and $T_{1/2\downarrow}$ values and a clear saturation of the lattice by HS units at high temperatures [see Fig. 7(b)]. The magnetization corresponding to the case of $J_0 = 100$ K, as displayed in the inset of Fig. 7(b), shows also hysteresis behavior with a clear saturation in the HS phase. Figures 8(a) and 8(b) show the behavior of the limiting transition temperatures $T_{1/2\uparrow}$ and $T_{1/2\downarrow}$ of the hysteresis loops as well as the associated equilibrium temperatures, defined as $T_{1/2} = \frac{1}{2}(T_{1/2\uparrow} + T_{1/2\downarrow})$ as function of the harmonic elastic constant A_0 and magnetic interaction J_0, respectively. The corresponding widths $\Delta T = T_{1/2\uparrow} - T_{1/2\downarrow}$ are also monitored when A_0 and J_0 increase. In Figs. 8(a) and 8(c), at low values of A_0 and for $J_0 = 50$ K, $\Delta T = 0$ K and only critical hysteresis cycles can be observed. There, the SCO lattice presents only gradual SCO transition and the magnetic subsystem exhibits only second-order phase transitions, where $T_{1/2\uparrow} \simeq T_{1/2\downarrow} \simeq T_{1/2}$. This is in fact the case for $A_0 = 10^3$ K nm^{-2} where one maximum is found for the response function χ in Fig. 3(c). With increasing A_0, one can

see from this figure that a second maximum appears in the low-temperature range. In this case, jumps are observed in the behavior of m, n_{HS}, and χ and thermal hysteresis loops take place, as we have already explained. From the above, the existence of a critical value of the interaction parameter A_0 is obvious [see Figs. 8(a) and 8(c)]. Close to this critical point, the upward borderline is slightly curved. This feature may account for the finite value of the temperature sweeping rate (kinetic effect) [50,77]. For $J_0 = 80$ K [Figs. 8(b) and 8(c)], the same behaviors are obtained with a decrease of the transition temperatures ($T_{1/2\uparrow}$, $T_{1/2\downarrow}$, and $T_{1/2}$) and an increase of hysteresis loop width as shown in Fig. 7(b). One also remarks that from the critical point, the hysteresis loop width increases gradually with the parameter A_0 and an almost straight lines are obtained [see Fig. 8(c)]. We now turn to the study of the spatiotemporal features of the SCO transformation obtained with this model. At this end, some snapshots of transient states have been taken along the thermal hysteresis loop in heating and cooling processes of Fig. 7(a) for the elastic constant value $A_0 = 8 \times 10^3$ K nm^{-2}. In this figure, one remarks that the transition from the LS to HS state (LS $\rightarrow$ HS) occurs around $T_4 = 75$ K on heating and from the HS to LS state (HS $\rightarrow$ LS) around $T_8 = 55$ K on cooling. Both processes proceed via nucleation phenomena with domain growth. The obtained results are summarized in Fig. 9 which shows, in addition to the nucleation and growth process of the HS (red/blue) and LS (green) spin domains in the model accompanied by the volume (here surface) change at the transition process, the clear occurrence of the magnetic order-disorder transition. As reported in Refs. [50–53,82,91–95] one can observe that the nucleation and growth processes of spin domains start from edges and corners for both HS $\rightarrow$ LS [Fig. 9: F(T_6)-A(T_1)] and LS $\rightarrow$ HS [Fig. 9: A(T_1)-F(T_6)] transitions. The growing domains propagate towards the center of the lattice and then merge. During HS $\rightarrow$ LS transformation, LS domains grow and finally combine together to extend to the whole system. Domain growth occurs in the diagonal directions and a few appear somewhere at the edges (see right panels of Fig. 9). The onset of such inhomogeneous structures was reported in Fig. 1 of Ref. [96] during the domain wall propagation observed by optical microscopy [17,48,49,72,73,77,93,96–109]. Following the process in heating from LS to HS phase, we also find local clusters of HS molecules (blue and red dots) around the corners, but in contrast to the case of the cooling branch, a large homogeneous region appears (see left panels of Fig. 9) as is observed with periodic boundary conditions (PBC), thus meeting the previous investigations of Nishino *et al.* [91], who pointed out the crucial role of the surface in the emergence of macroscopic domain nucleation in the elastic models. It is important to mention in passing that years ago a hybrid model combining short-range Ising coupling and elastic long-range interactions was proposed by Nakada *et al.* [110] who demonstrated that an inhomogeneous configuration (lattice and spin degrees of freedom) are also observed at critical temperature T_c when the SCO atoms interact in a lattice with periodic boundary conditions.

A possible reason for this difference on cooling and heating processes originates from the energy and entropy gain. In the cooling process at low temperatures, the energy stability is more important than the entropy gain and the nucleation
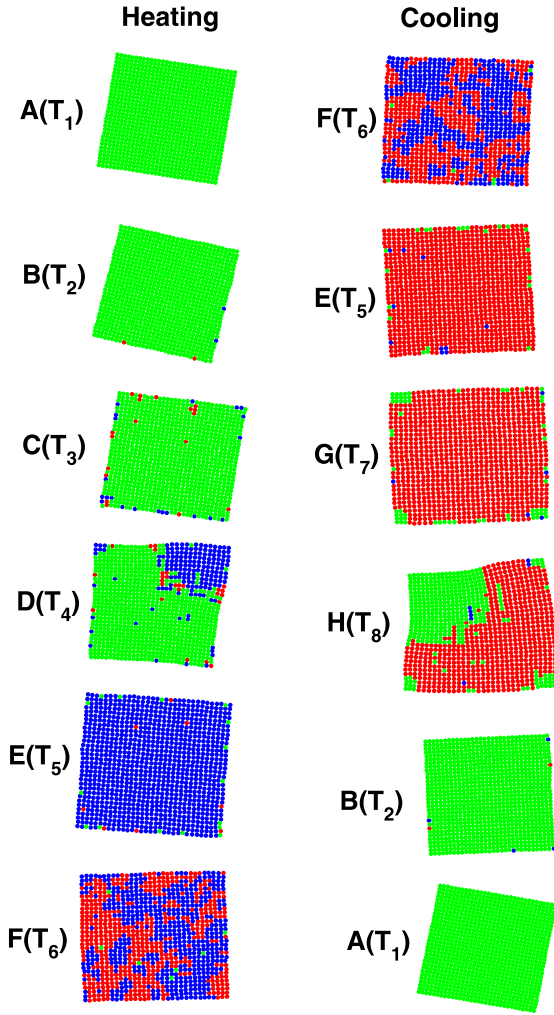
Heating   **Cooling**

FIG. 9. Snapshots of lattice configuration for 32×32 system, along the thermal hysteresis loop of Fig. 7(a), with $A_0 = 8 \times 10^3 \ \mathrm{K \, nm^{-2}}$, during heating (left panels) and cooling (right panels) processes, at different temperatures $T_1 = 26$ K, $T_2 = 54$ K, $T_3 = 74$ K, $T_4 = 75$ K, $T_5 = 76$ K, $T_6 = 126$ K, $T_7 = 56$ K, and $T_8 = 55$ K. Green clusters are associated to those of LS units whereas red (spin $+1$) and blue (spin -1) dot clusters consist of HS unit clusters. It is clear that the nucleation and growth process start from corners, and edges with deformations, and then propagated through the crystal. Values considered for other model parameters are $J_0 = 50$ K, $\alpha = 100 \ \mathrm{K \, nm^{-1}}$, $\Delta = 450$ K, and $g = 150$.

from the corner is the most favorable. However, in the heating process at high temperatures, the entropy gain becomes more important and the configuration may change uniformly, which can be seen in the inner part of the system. This obviously indicates that once the system reaches the saturated HS phases, the magnetic interaction between the HS units becomes dominant compared to the elastic interactions.

Furthermore, following the same procedure as that developed in Ref. [50], the nucleation and growth processes from the corners in our model can be explained by simple energetic considerations. During HS $\rightarrow$ LS transition, for example, let us start from a lattice with a saturated HS state and consider a nucleus made of a single LS site. The energy cost associated with the creation of an LS nucleus at the corner, edge, and

center of the HS lattice defined by $\Delta E = E(\mathrm{LS}) - E(\mathrm{HS})$ reads as

$$\Delta E_{\mathrm{corner}}(\mathrm{HS} \rightarrow \mathrm{LS})$$
$$= -[\Delta - k_B T \ln(g)] + 2J_0 + 4(A_0 + B_0)R_1^2, \quad (15)$$

$$\Delta E_{\mathrm{edge}}(\mathrm{HS} \rightarrow \mathrm{LS})$$
$$= -[\Delta - k_B T \ln(g)] + 3J_0 + 2(3A_0 + 4B_0)R_1^2, \quad (16)$$

$$\Delta E_{\mathrm{center}}(\mathrm{HS} \rightarrow \mathrm{LS})$$
$$= -[\Delta - k_B T \ln(g)] + 4J_0 + 8(A_0 + 2B_0)R_1^2. \quad (17)$$

The analysis of these equations clearly shows that while the system wins electronic energy (especially at very low temperature) during the spin flip from HS to LS, it also faces an energy barrier originating from the magnetic and the elastic interactions, whose contributions can be easily identified in the previous equations. The interesting point here is that the magnetic and the ligand-field energies compete (in the case of ferromagnetic interactions) and it is clearly seen that the magnetic interactions stabilize the HS phase, by increasing the energy barrier. Moreover, both of these contributions increase when going from corner to edge and then to a bulk site. As a result, the probability of appearance of a LS state along the cooling process ($\sim e^{-\beta \Delta E}$) is higher for corner atoms. This justifies the nucleation and growth of spin domains from the corner of lattice. For LS $\rightarrow$ HS transition, similar considerations have been developed. We start from a LS lattice in which we flip a corner, edge, or central site form LS to HS. The following energy barriers are found for each case as

$$\Delta E_{\mathrm{corner}}(\mathrm{LS} \rightarrow \mathrm{HS}) = \Delta - k_B T \ \ln(g) + 4(A_0 + B_0)R_1^2$$
$$+ 64(A_1 + 2B_1)R_1^4, \quad (18)$$

$$\Delta E_{\mathrm{edge}}(\mathrm{LS} \rightarrow \mathrm{HS}) = \Delta - k_B T \ \ln(g) + 2(3A_0 + 4B_0)R_1^2$$
$$+ 32(3A_1 + 8B_1)R_1^4, \quad (19)$$

$$\Delta E_{\mathrm{center}}(\mathrm{LS} \rightarrow \mathrm{HS}) = \Delta - k_B T \ \ln(g) + 8(A_0 + 2B_0)R_1^2$$
$$+ 128(A_1 + 4B_1)R_1^4 \quad (20)$$

in which the elastic energy part remains unchanged because of its positive character with a weak additional term in R_1^4, while the ligand-field contributions changed their signs and the magnetic part vanished. Adopting the same energetic reasoning, here again, the energy barrier at the corner is the smallest one and so the nucleation will start from the corner sites. Compared with the cooling process, the heating one shows large thermal fluctuations which favor the probabilities of nucleation at the center and at the edges. However, nucleation from the corners remains the most likely. This nucleation from the corners can be explained by the fact that the SCO units located at the corners of the crystal relax the elastic stresses more easily on the surface because of their smaller number of neighbors.

F. Isothermal relaxation near the hysteresis loop

Here, we investigated the nonequilibrium properties of the system, at various temperatures ($T = 30, 45, 50,$ and 54 K)
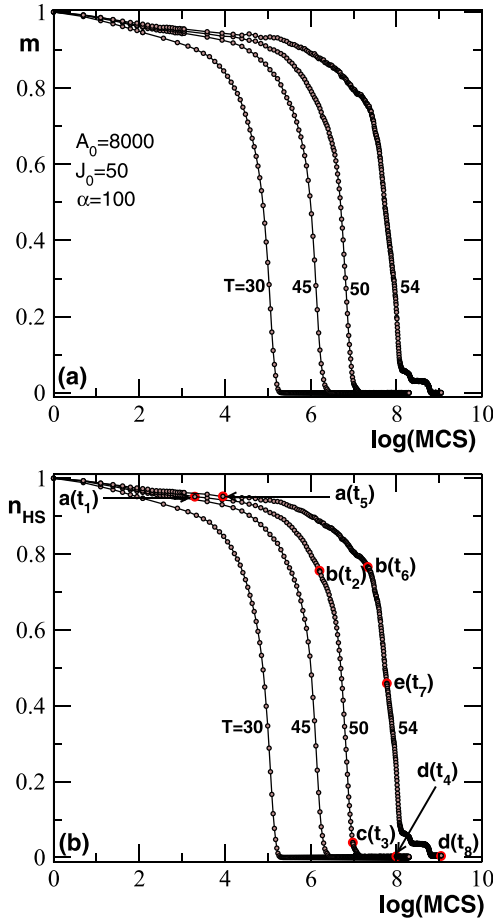
FIG. 10. Isothermal relaxation curves of 32×32 system, near the thermal hysteresis loop of Fig. 7(a), for $A_0 = 8 \times 10^3$ K nm^{-2}, at different temperatures: $T = 30, 45, 50$, and 54 K. Relaxation time increases with temperature, and concave curves are gotten from its initial stage. Red circular dots in (b) indicate the position of spatiotemporal configurations in Fig 11, along the relaxation curves for $T = 50$ and 54 K. Other model parameters are the same in Fig. 7(a) with $A_0 = 8 \times 10^3$ K nm^{-2}.

near the thermal hysteresis loop of Fig. 7(a) using an elastic constant $A_0 = 8000$ K nm^{-2}. Interesting relaxation dynamics of metastable states are obtained according to values of model parameters. In experiments, after photoirradiation to a long-lived HS state, by means of light-induced excited spin-state trapping (LIESST) [26,111–113], even that saturates HS fraction n_{HS}, the relaxation process is visualized at low temperatures or by rapid quenching of the high-temperature stable HS state. Using the same algorithm described in Sec. III, we performed the simulations starting from a fully HS state, on a square lattice ($L = 32$), and used 25 independent runs. The obtained results are illustrated in Fig. 10, where the magnetization m [Fig. 10(a)] and the HS fraction n_{HS} [Fig. 10(b)] evolve according to the Monte Carlo steps (MCS). Typical one-step relaxation curves are obtained and the behaviors of m and n_{HS} bear some resemblance. At low temperatures, from the hysteresis loop, sigmoidal curves are observed. From the outside to the interior of the loop, one remarks that the relaxation time increases when the temperature increases
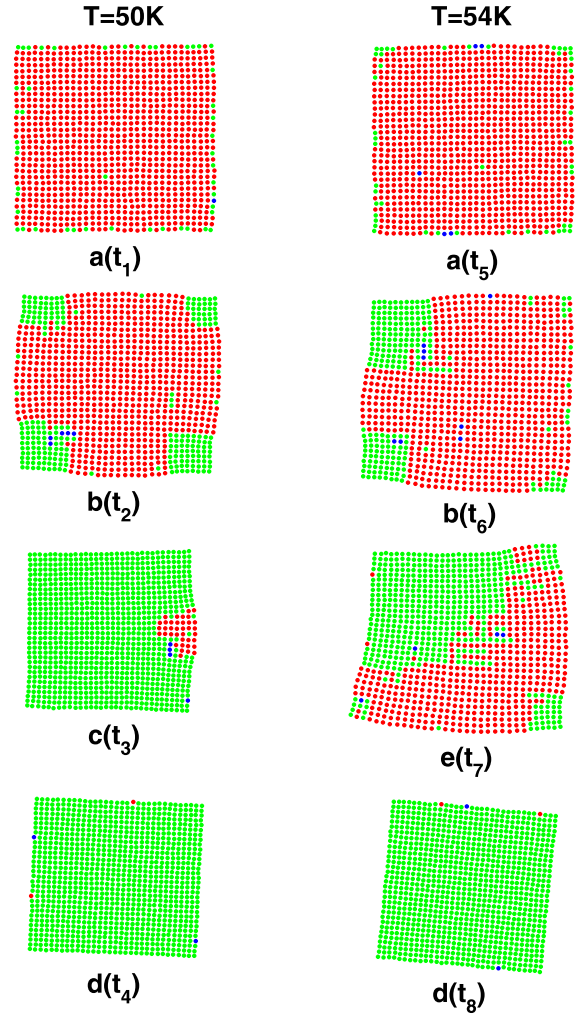

FIG. 11. Snapshots of lattice configuration, along the relaxation process for two temperatures $T = 50$ K (left panels) and $T = 54$ K (right panels) at different simulation times: $t_1 = 27$, $t_2 = 496$, $t_3 = 1080$, $t_4 = 2980$, $t_5 = 52$, $t_6 = 1528$, $t_7 = 2386$, and $t_8 = 8456$ MCS. Colors have the same meaning as in Fig. 9. Horizontal panels correspond to the same coverage n_{LS} of LS fraction, except for $c(t_3)$ and $e(t_7)$ configurations, while the configurations of vertical panels have been taken at the same temperature T. LS nuclei are formed from corners and edges, and grow to coalesce at high coverage. In (a)–(e), respectively, 5%, 23%, 96%, 99%, and 53% of lattices are occupied by LS units. Values considered for other model parameters are $A_0 = 8 \times 10^3$ K nm^{-2}, $J_0 = 50$ K, $\alpha = 100$ K nm^{-1}, $\Delta = 450$ K, and $g = 150$.

as reported in literature [50,77,79,80]. This counterintuitive behavior, where the relaxation process of a metastable (or unstable) state slows down as the temperature increases, is due to the proximity of the lower branch of the thermal hysteresis, in which the HS state is thermodynamically stable, and so it has a long lifetime.

Figure 11 shows some transient states, taken also along the relaxation curves, at different simulation times, and temperatures $T = 50$ and 54 K. Horizontally, snapshots are obtained at the same coverage or concentration $n_{LS}(=1 - n_{HS})$ of LS units excepted for panels $c(t_3)$ and $e(t_7)$. Vertically, they correspond to the same simulation temperature T. The same

qualitative characteristics of clustering of LS domains were also observed in isothermal relaxation processes, from the metastable HS phase at the vicinity of the thermal hysteresis loop (see Fig. 11). On the other hand, all HS units have the same probability to switch from HS state to LS state during the HS $\rightarrow$ LS transition, followed by a volume decrease. Very close to the thermal hysteresis loop (see right panels of Fig. 11 where $T = 54$ K), one gets uniform aggregates of HS states, with some isolated LS units almost in their edges at the initial stage of the relaxation process. It is clear that, according to previous elastic model with open boundary conditions on 2D circular crystal, Nishino *et al.* [114] show that homogeneous macroscopic nucleation events occurred with long-range interactions for which single-domain nucleation appears along the relaxation processes. As for the homogeneous transformation of the magnetic system, while the magnetoelastic coupling contains both short- and long-range effects, as we explained the long-range effects of $J(r_{ij})$ depend on the quantity $\alpha(r_{ij} - R_{eq}^{HH})$ which is negligible in the HS region where the magnetic interactions are acting. Here, at different simulation times and fixed temperature, LS units are created and the domain growth is clearly observed from the corners as well as at the edges of the lattice configuration. Domain growth occurs in the diagonal directions, and a few appear somewhere at the edges as previously observed in the right panels of Fig. 9 (on cooling process). This happens by the way of the low-cost energetic associated with the creation of an LS nucleus at the edges and mostly from the corners. These results are consistent and show good agreement.

V. CONCLUSION

A deformable lattice SCO model with ferromagnetic interactions is presented. It allows to reproduce thermal and spatiotemporal behaviors of SCO solids and Prussian blue analogs (PBAs). The system of SCO compounds study is mapped on the Blume-Emery-Griffiths model with three states ($S = \pm 1, 0$), where $S = \pm 1$ denote the magnetic HS state and $S = 0$ is associated to the diamagnetic LS state. These atoms interact elastically with their NN and NNN via anharmonic springs, whose elastic constants depend on their distances. Moreover, the NN sites also interact magnetically with an exchange interaction, whose value is a function of the in-stantaneous distance between the spin states. As a result, the magnetic interaction between the spin states depends on the elastic properties of the lattice. In the magnetic ordering, only HS atoms, with $S = \pm 1$, interact in the HS phase, while the spin transition occurs between HS ($S = \pm 1$) and LS ($S = 0$) states. Finite-size effects have been detected at finite temperature on the model. This mapping allowed us to construct the phase diagrams of the model, from which gradual and first-order transitions are obtained, and on which the effects of the model interaction parameters are analyzed. The thermal dependence of the lattice configuration is studied upon heating and cooling along the thermal hysteresis loop with model parameters. This characterized the evolution of the system at a constant temperature, and revealed the mechanism of the nucleation and growth processes of the HS and LS phases as well as the organization of the magnetic state. The isothermal low-temperature relaxation of the metastable HS states is also studied for which macroscopic nucleation phenomena were also identified. Compared to the previous elastic models, the present model has the advantage of producing a richer landscape of phase transitions according to the interaction between the magnetic and the lattice subsystems. In particular, we found that the magnetic interactions act in an efficient way on the elastic properties of the lattice by changing the thermal evolution of the average lattice bond length in the HS state, while their effect is very limited on the HS fraction. All these results suggest that the electroelastic models can be extended to investigate the problem of magnetoelastic interactions in PBAs and other related SCO materials with magnetic interactions. Extensions of this model considering antiferromagnetic interactions instead of ferromagnetic ones, or other lattice topology leading to magnetic frustration, might constitute an interesting extension of this work.

[1] P. Gütlich and Harold A. Goodwin, *Spin-Crossover in Transition Metal Compounds I, II and III* (Springer, Berlin, 2004), pp. 233–235.

[2] J. Linares, E. Codjovi, and Y. Garcia, Sensors **12**, 4479 (2012).

[3] A. Bousseksou, G. Molnàr, L. Salmon, and W. Nicolazzi, Chem. Soc. Rev. **40**, 3313 (2011).

[4] P. Gütlich, A. B. Gaspar, and Y. Garcia, Beilstein J. Org. Chem. **9**, 342 (2013)

[5] M. Cavallini and M. Melucci, ACS Appl. Mater. Interfaces **7**, 16897 (2015).

[6] D. Gentili, N. Demitri, B. Schäfer, F. Liscio, I. Bergenti, G. Ruani, M. Ruben, and M. Cavallini, J. Mater. Chem. C **3**, 7836 (2015).

[7] A. D. Naik, K. Robeyns, C. F. Meunier, A. F. Léonard, A. Rotaru, B. Tinant, Y. Filinchuk, B. L. Su, and Y. Garcia, Inorg. Chem. **53**, 1263 (2014).

[8] P. Lloveras, E. Stern-Taulats, M. Barrio, J. L. Tamarit, S. Crossley, W. Li, V. Pomjakushin, A. Planes, L. Mañosa, N. D. Mathur, and X. Moya, Nat. Commun. **6**, 8801 (2015).

[9] P. J. von Ranke, Appl. Phys. Lett. **110**, 181909 (2017).

[10] X. Zhang, T. Palamarciuc, J.-F. Letard, P. Rosa, E. V. Lozada, F. Torres, L. G. Rosa, B. Doudin, and P. A. Dowben, Chem. Commun. **50**, 2255 (2014)

[11] M. Hiroyuki, K. Keita, and K. Nobuo, Chem. Lett. **37**, 446 (2008).

[12] C. Piguet, E. Rivara-Minten, G. Hopfgartner, and J.-C. G. Bünzli, Helv. Chim. Acta **78**, 1541 (1995).

[13] C. Piguet, E. Rivara-Minten, G. Bernardinelli, J.-C. G. Bünzli, and G. Hopfgartner, J. Chem. Soc., Dalton Trans. **3**, 421 (1997).

[14] C. Edder, C. Piguet, J. C. G. Bünzli, and G. Hopfgartner, Chem. Eur. J. **7**, 3014 (2001)

[15] K. Boukheddaden, M. H. Rotti, G. Bouchez, M. Sy, M. M. Dîrtu, M. Parlier, J. Linares, and Y. Garcia, J. Phys. Chem. C **122**, 7597 (2018).

[16] H. J. Shepherd, I. A. Gural'Skiy, C. M. Quintero, S. Tricard, L. Salmon, G. Molnár, and A. Bousseksou, Nat. Commun. **4**, 2607 (2013)

[17] M. Sy, D. Garrot, A. Slimani, M. Paez-Espejo, F. Varret, and K. Boukheddaden, Angew. Chem. Int. Ed. **55**, 1755 (2016)

[18] M. D. Manrique-Juarez, S. Rat, F. Mathieu, D. Saya, I. Séguy, T. Leïchlé, L. Nicu, L. Salmon, G. Molnár, and A. Bousseksou, Appl. Phys. Lett. **109**, 061903 (2016).

[19] E. König and B. Kanellakopulos, Chem. Phys. Lett. **12**, 485 (1972).

[20] P. Gütlich, A. Hauser, and H. Spiering, Angew. Chem. Int. Ed. **33**, 2024 (1994).

[21] O. Kahn and G. P. Launay, Chemtronics **3**, 140 (1988).

[22] C. P. Köhler, R. Jacobi, E. Meissner, L. Wiehl, H. Spiering, and P. Gütlich, J. Phys. Chem. Solids **51**, 239 (1990).

[23] H. Tokoro, S.-I. Ohkoshi, and K. Hashimoto, Appl. Phys. Lett. **82**, 1245 (2003).

[24] D. A. Pejaković, J. L. Maison, C. Kitamura, J. S. Miller, and A. J. Epstein, Polyhedron **20**, 1435 (2001).

[25] K. Kato, Y. Moritomo, M. Takata, M. Sakata, M. Umekawa, N. Hamada, S. Ohkoshi, H. Tokoro, and K. Hashimoto, Phys. Rev. Lett. **91**, 255502 (2003)

[26] F. Varret, K. Boukheddaden, C. Chong, A. Goujon, B. Gillon, J. Jeftic, and A. Hauser, Eur. Phys. Lett. **77**, 30007 (2007)

[27] H. Banerjee, S. Chakraborty, and T. Saha-Dasgupta, Inorganics **5**, 47 (2017).

[28] A. Gîndulescu, A. Rotaru, J. Linares, M. Dimian, and J. Nasser, J. Phys: Conf. Ser. **268**, 012007 (2011).

[29] M. Nishino, S. Miyashita, and P. A. Rikvold, Phys. Rev. B **96**, 144425 (2017).

[30] C. Enachescu, L. Stoleriu, A. Stancu, and A. Hauser, Phys. Rev. B **82**, 104114 (2010).

[31] M. Sorai and S. Seki, J. Phys. Chem. Solids **35**, 555 (1974).

[32] M. Paez-Espejo, M. Sy, and K. Boukheddaden, J. Am. Chem. Soc. **138**, 3202 (2016).

[33] L. G. Lavrenova and O. G. Shakirova, Eur. J. Inorg. Chem. **2013**, 670 (2013).

[34] K. Affes, A. Slimani, Y. Singh, A. Maalej, and K. Boukheddaden, J. Phys.: Condens. Matter **32**, 255402 (2020).

[35] B. Benaicha, K. Van Do, A. Yangui, N. Pittala, A. Lusson, M. Sy, G. Bouchez, H. Fourati, C. J. Gómez-Garcia, S. Triki, and K. Boukheddaden, Chem. Sci. **10**, 6791 (2019)

[36] Y. Garcia, F. Robert, A. D. Naik, G. Zhou, B. Tinant, K. Robeyns, S. Michotte, and L. Piraux, J. Am. Chem. Soc. **133**, 15850 (2011).

[37] C.-F. Wang, R.-F. Li, X.-Y. Chen, R.-J. Wei, L.-S. Zheng and J. Tao, Angew. Chem., Int. Ed. **54**, 1574 (2015).

[38] C. F. Wang, M. J. Sun, Q. J. Guo, Z. X. Cao, L. S. Zheng, and J. Tao, Chem. Commun. **52**, 14322 (2016).

[39] M. Hasegawa, F. Renz, T. Hara, Y. Kichuki, Y. Fukada, J. Okubo, T. Hoshi, and W. Linert, Chem. Phys. **277**, 21 (2002).

[40] R. González-Prieto, B. Fleury, F. Schramm, G. Zoppellaro, R. Chandrasekar, O. Fuhr, S. Lebedkin, M. Kappes, and M. Ruben, Dalton Trans. **40**, 7564 (2011).

[41] J.-L. Wang, Q. Liu, Y.-S. Meng, X. Liu, H. Zheng, Q. Shi, C.-Y. Duan, and T. Liu, Chem. Sci. **9**, 2892 (2018).

[42] C.-F. Wang, G.-Y. Yang, Z.-S. Yao, and J. Tao, Chem. Eur. J. **24**, 3218 (2018)

[43] L. Salmon, G. Molnár, D. Zitouni, C. Quintero, C. Bergaud, J.-C. Micheau, and A. Bousseksou, J. Mater. Chem. **20**, 5499 (2010).

[44] S. Titos-Padilla, J. M. Herrera, X. W. Chen, J. J. Delgado and E. Colacio, Angew. Chem., Int. Ed. **50**, 3290 (2011).

[45] C. Lochenie, K. Schötz, F. Panzer, H. Kurz, B. Maier, F. Puchtler, S. Agarwal, A. Köhler, and B. Weber, J. Am. Chem. Soc. **140**, 700 (2018)

[46] J. Yuan, S.-Q. Wu, M.-J. Liu, O. Sato, and H.-Z. Kou, J. Am. Chem. Soc. **140**, 9426 (2018)

[47] S. B. Ogou, T. D. Oke, F. Hontinfinde, and K. Boukheddaden, Adv. Theory Simul. **2**, 1800192 (2019)

[48] M. Nishino, K. Boukheddaden, S. Miyashita, and F. Varret, Phys. Rev. B **72**, 064452 (2005).

[49] K. Boukheddaden, M. Nishino, S. Miyashita, and F. Varret, Phys. Rev. B **72**, 014467 (2005)

[50] A. Slimani, K. Boukheddaden, F. Varret, H. Oubouchou, M. Nishino, and S. Miyashita, Phys. Rev. B **87**, 014111 (2013).

[51] A. Slimani, K. Boukheddaden, and K. Yamashita, Phys. Rev. B **92**, 014111 (2015).

[52] M. Ndiaye and K. Boukheddaden, J. Phys. Soc. Jpn. **89**, 014004 (2020).

[53] M. Nishino and S. Miyashita, Phys. Rev. B **88**, 014108 (2013).

[54] K. Boukheddaden, R. Traiche, H. Oubouchou, and J. Linares, Magnetochemistry **2**, 17 (2016).

[55] M. Paez-Espejo, M. Sy, and K. Boukheddaden, J. Am. Chem. Soc. **140**, 11954 (2018).

[56] A.-I. Popa, L. Stoleriu, and C. Enachescu, J. Appl. Phys. **129**, 131101 (2021)

[57] H. Oubouchou, Y. Singh, and K. Boukheddaden, Phys. Rev. B **98**, 014106 (2018).

[58] Y. Singh, H. Oubouchou, M. Nishino, S. Miyashita, and K. Boukheddaden, Phys. Rev. B **101**, 054105 (2020).

[59] A. Slimani, K. Boukheddaden, and K. Yamashita, Phys. Rev. B **89**, 214109 (2014).

[60] K. Affes, A. Slimani, A. Maalej, and K. Boukheddaden, Chem. Phys. Lett. **718**, 46 (2019).

[61] A. Slimani and K. Boukheddaden, Phys. Chem. Chem. Phys. **20**, 28583 (2018).

[62] H. Oubouchou, A. Slimani, and K. Boukheddaden, Phys. Rev. B **87**, 104104 (2013).

[63] E. Milin, V. Patinec, S. Triki, E.-E. Bendeif, S. Pillet, M. Marchivie, G. Chastanet, and K. Boukheddaden, Inorg. Chem. **55**, 11652 (2016).

[64] M. Ndiaye, S. Pillet, E.-E. Bendeif, M. Marchivie, G. Chastanet, K. Boukheddaden, and S. Triki, Eur. J. Inorg. Chem. **2018**, 305 (2018).

[65] D. Chiruta, J. Linares, M. Dimian, Y. Alayli, and Y. Garcia, Eur. J. Inorg. Chem. **2013**, 5086 (2013).

[66] C. Enachescu and W. Nicolazzi, C. R. Chimie **21**, 1179 (2018).

[67] C. Timm and C. J. Pye, Phys. Rev. B **77**, 214437 (2008)

[68] D. Silva and P. A. Rikvold, Phys. Chem. Chem. Phys. **21**, 6216 (2019).

[69] M. Reczyński, D. Pinkowicz, K. Nakabayashi, C. Näther, J. Stanek, M. Kozieł, J. Kalinowska-Tłuścik, B. Sieklucka, S.-I. Ohkoshi, and B. Nowicka, Angew. Chem. Int. Ed. **60**, 2330 (2020).

[70] M. Nishino, K. Boukheddaden, S. Miyashita, and F. Varret, Polyhedron **24**, 2852 (2005).

[71] M. Nishino, K. Boukheddaden, S. Miyashita, and F. Varret, Phys. Rev. B **68**, 224402 (2003).

[72] S. Mouri, K. Tanaka, S. Bonhommeau, N. O. Moussa, G. Molnár, and A. Bousseksou, Phys. Rev. B **78**, 174308 (2008)

[73] K. Ridier, G. Molnár, L. Salmon, W. Nicolazzi, and A. Bousseksou, Solid State Sci. **74**, A1 (2017)

[74] E. Collet and P. Guionneau, C. R. Chimie **21**, 1133 (2018)

[75] J. Pavlik, W. Nicolazzi, G. Molnár, R. Boca, and A. Bousseksou, Eur. Phys. J. B **86**, 292 (2013).

[76] T. Nakamoto, Z.-C. Tan, and M. Sorai, Inorg. Chem. **40**, 3805 (2001)

[77] K. Boukheddaden, I. Shteto, B. Hôo, and F. Varret, Phys. Rev. B **62**, 14796 (2000); K. Boukheddaden, I. Shteto, B. Horomano, and F. Varret, *ibid.* **62**, 14806 (2000) and references therein.

[78] T. D. Oke, F. Hontinfinde, and K. Boukheddaden, Eur. Phys. J. B **86**, 271 (2013) and references therein.

[79] T. D. Oke, F. Hontinfinde, and K. Boukheddaden, Appl. Phys. A **120**, 309 (2015).

[80] T. D. Oke, F. Hontinfinde, and K. Boukheddaden, Comput. Condens. Matter **9**, 27 (2016)

[81] W. Nicolazzi, S. Pillet, and C. Lecomte, Phys. Rev. B **78**, 174401 (2008).

[82] W. Nicolazzi, J. Pavlik, S. Bedoui, G. Molnár, and A. Bousseksou, Eur. Phys. J. Topics **222**, 1137 (2013)

[83] A. Real, J. Zarembowitch, O. Kahn, and X. Solans, Inorg. Chem. **26**, 2939 (1987)

[84] D.-Y. Wu, O. Sato, Y. Einaga, and C.-Y. Duan, Angew. Chem. Int. Ed. **48**, 1475 (2009)

[85] V. E. Vorobeva, N. E. Domracheva, A. V. Pyataev, M. S. Gruzdev, and U. V. Chervonova, Low Temp. Phys. **41**, 15 (2015)

[86] S.-G. Wu, Md. N. Hoque, J.-Y. Zheng, G.-Z. Huang, N. Vu Ha Anh, L. Ungur, W.-X. Zhang, Z.-P. Ni, and M.-L. Tong, CCS Chem. **2**, 453 (2020).

[87] C. D. Mekuimemba, F. Conan, A. J. Mota, M. A. Palacios, E. Colacio, and S. Triki, Inorg. Chem. **57**, 2184 (2018).

[88] T. Liu, H. Zheng, S. Kang, Y. Shiota, S. Hayami, M. Mito, O. Sato, K. Yoshizawa, S. Kanegawa, and C. Duan, Nat Commun **4**, 2826 (2013).

[89] H.-Y. Sun, Y.-S. Meng, and T. Liu, Chem. Commun. **55**, 8359 (2019)

[90] I. M. Karandashev, B. V. Kryzhanovsky, and M. Y. Malsagov, Opt. Mem. Neural Networks **26**, 165 (2017)

[91] M. Nishino, C. Enachescu, S. Miyashita, K. Boukheddaden, and F. Varret, Phys. Rev. B **82**, 020409(R) (2010).

[92] C. Enachescu, M. Nishino, S. Miyashita, A. Hauser, A. Stancu, and R. Stoleriu, Eur. Phys. Lett. **91**, 27003 (2010).

[93] M. Nishino, K. Boukheddaden, S. Miyashita, and F. Varret, Phys. Rev. B **74**, 214416 (2006).

[94] C. Enachescu, M. Nishino, S. Miyashita, K. Boukheddaden, F. Varret, and P. A. Rikvold, Phys. Rev. B **91**, 104102 (2015).

[95] C. Enachescu, M. Nishino, S. Miyashita, L. Stoleriu, and A. Stancu, Phys. Rev. B **86**, 054114 (2012)

[96] A. Slimani, F. Varret, K. Boukheddaden, C. Chong, H. Mishra, J. Haasnoot, and S. Pillet, Phys. Rev. B **84**, 094442 (2011).

[97] Y. Ogawa, S. Koshihara, K. Koshino, T. Ogawa, C. Urano, and H. Takagi, Phys. Rev. Lett. **84**, 3181 (2000).

[98] K. Boukheddaden, J. Linares, H. Spiering, and F. Varret, Eur. Phys. J. B **15**, 317 (2000)

[99] M. Nishino and S. Miyashita, Phys. Rev. B **63**, 174404 (2001)

[100] H. Watanabe, N. Bréfuel, S. Mouri, J.-P. Tuchagues, E. Collet and Tanaka, Eur. Phys. Lett. **96**, 17004 (2011).

[101] K. Boukheddaden, M. Sy, M. Paez-Espejo, A. Slimani, and F. Varret, Phys. B (Amsterdam) **486**, 187 (2016).

[102] M. Paez-Espejo, M. Sy, F. Varret, and K. Boukheddaden, Phys. Rev. B **89**, 024306 (2014).

[103] C. Chong, F. Varret, and K. Boukheddaden, Phys. Rev. B **81**, 014104 (2010).

[104] C. Enachescu, R. Tanasa, A. Stancu, F. Varret, J. Linares, and E. Codjovi, Phys. Rev. B **72**, 054413 (2005)

[105] K. Boukheddaden, Eur. J. Inorg. Chem. **2013**, 865 (2013).

[106] B. Hôo, K. Boukheddaden, and F. Varret, Eur. Phys. J. B **17**, 449 (2000)

[107] A. Slimani, F. Varret, K. Boukheddaden, D. Garrot, H. Oubouchou, and S. Kaizaki, Phys. Rev. Lett. **110**, 087208 (2013).

[108] H. Romstedt, A. Hauser, and H. Spiering, J. Phys. Chem. Solids **59**, 265 (1998).

[109] K. Boukheddaden, F. Varret, S. Salinke, J. Linares, and E. Codjovi, Phase Transitions **75**, 733 (2002)

[110] T. Nakada, T. Mori, S. Miyashita, M. Nishino, S. Todo, W. Nicolazzi, and P. A. Rikvold, Phys. Rev. B **85**, 054408 (2012)

[111] S. Descurtins, P. Gütlich, K. M. Hasselbach, A. Hauser, and H. Spiering, Inorg. Chem. **24**, 2174 (1985).

[112] A. Hauser, Coord. Chem. Rev. **111**, 275 (1991).

[113] Y. Ogawa, T. Ishikawa, S. Koshihara, K. Boukheddaden, and F. Varret, Phys. Rev. B **66**, 073104 (2002)

[114] M. Nishino, C. Enachescu, S. Miyashita, P. A. Rikvold, K. Boukheddaden, and F. Varret, Sci. Rep. **1**, 162 (2011)